APPLIED RESEARCH

Real-Time Emulation of a PMSM-Loaded MMC With BESS

ALAA OMAR, (Student Member, IEEE), **ALAN WOOD**, (Member, IEEE),
HAMISH LAIRD, (Senior Member, IEEE), **AND PAUL GAYNOR**, (Member, IEEE)
Department of Electrical and Computer Engineering, University of Canterbury, Christchurch 8041, New Zealand

Corresponding author: Alaa Omar (alaa.omar@pg.canterbury.ac.nz)

ABSTRACT This paper details a validated real-time emulation of a modular multilevel converter with integrated energy storage sub-modules. The real-time emulated system is implemented using *MicroLabBox/dSPACE*. A validation is carried out by constructing and testing a prototype of the converter with a reduced number of voltage levels and integrated batteries. The real-time operation of the emulated converter is tested under a range of loading conditions and compared to the prototype. Emulated results closely match the physical prototype results. Based on this outcome, a converter that comprises a high number of sub-modules is emulated and investigated when connected to a large scale motor. This research provided a seamless extension of the model from a lower to a higher number of converter sub-modules with minor changes in the emulation structure, the basic control and the sorting algorithm. This is a novel real-time emulation of the converter that can be used for electric vehicle application using *MicroLabBox/dSPACE*.

INDEX TERMS Battery, electric vehicle, emulation, FPGA, HIL, modular multilevel converter, real-time, state of charge.

I. INTRODUCTION

The modular multilevel converter (MMC) has beneficial features due to its redundancy and scalability. These features make the converter an attractive alternative for medium voltage drives [1], [2]. The MMC is also utilised in HVDC transmission systems [3], and power quality improvements [4]. The number of voltage levels or sub-modules (SMs) in an MMC arm varies according to the application. Typically in the HVDC application, an MMC comprises hundreds of SMs per arm [5]. An extended application of the MMC is to replace the SM capacitor with a battery energy storage system (BESS). The MMC-BESS topology has recently been investigated as a centralised traction converter in electric vehicles [6], [7]. A laboratory prototype of such a converter gives insights into the expected behaviour of the MMC-BESS system; however, it is not feasible to construct a full-scale converter with a large number of SMs at early stages of research. Therefore, researchers use simulation tools to analyse larger converter performance and to develop suitable control methods.

Various simulation tools such as MATLAB, PSCAD, and PLECS can be utilised to analyse MMC behaviour [8]. This is very helpful during early stages of the research and development phase; yet the fidelity of simulations is low as shown in Fig. 1 [9]. Simulation can be regarded as tier 1 in fidelity levels and physical prototype testing can be defined as tier 3. A tier 2 in the fidelity levels is the hardware in the loop (HIL) method [10]. HIL testing methods can be classified into two categories; the controller hardware in the loop (CHIL) and power hardware in the loop (PHIL). When a controller is interfaced with an emulation platform that can process the dynamics of a specific system in real-time, the HIL testing arrangement is called CHIL. There are no physical devices in CHIL. For the other category, the PHIL methodology implies that the emulation platform is connected (via communication or physical I/Os) to external physical components.

Considering their implementation environment or platforms, real-time emulation of electrical systems can be implemented using field-programmable gate arrays (FPGAs)

or CPUs. Parallel operation of FPGAs enables a faster calculation time compared to CPUs [11]. FPGAs can capably emulate real-time systems down to the range of hundreds of nanoseconds. However, the availability of FPGA resources determines the complexity and scale of the designs that can be implemented on the FPGA. For MMCs, real-time simulation of the converter with a capacitor in each sub-module was investigated in the literature [11], [12], [13], [14]. OPAL RT-LAB has been used to validate factory acceptance tests of MMCs in HVDC applications [15], [16]. Commercial HIL platforms from Typhoon HIL, dSPACE, RT Box, and Speedgoat offer many products that can be utilised as a HIL platform. RT Box and Typhoon HIL use the state-space matrix representation to run the converter and application real-time models [14]. The Mission Profile Emulator of MMC-BESS was previously studied using a full-bridge converter to emulate the arm current, without incorporating the batteries model [17]. Another study proposed the real-time operation of the MMC-BESS using the state space model of the converter and a lookup table method [18]. The study was presented concurrently with the preliminary results of the work presented in this manuscript [19]. The current work features a modular and generic sorting algorithm that is easily extendable and is based on logic sorting rather than a PI controller as proposed in [18]. The real-time emulation in this paper, is a novel implementation of a CHIL emulation of a MMC-BESS and an extension of our work presented in [19], to validate motor real-time operation compared to a prototype MMC-BESS.

In this research, *MicroLabBox/dSPACE* is used as the emulation platform of the MMC-BESS control and motor dynamics. *MicroLabBox* is typically used as a rapid proto-typing controller for fast implementation of control systems using Simulink/Matlab interface. However, no dedicated physical library blocks (switches or batteries) are available to implement the real-time emulation of the converter using *MicroLabBox*. Thus, the converter dynamic model equations and batteries model are used to emulate the converter performance in real-time. The Math library, Matlab functions of Simulink, and real-time IO interfaces provided by dSPACE are used to build the real-time application using Matlab/Simulink. The Simulink Coder is utilised to generate C code for the real-time hardware, which is downloaded and executed on the *MicroLabBox*. The *MicroLabBox* architecture includes a local bus that connects the DS1202 (real-time processor) and the DS1302 (FPGA) for processing input/output signals, thereby reducing the calculation load on the real-time processor and ensuring real-time implementation without any task overrun. The developed system is capable of emulating the dynamic performance of 80 SMs/arm with a sampling time of 80 μs. Switches are ideally represented to facilitate the extension of the converter to a large number of levels without task overrun nor significantly increasing the sampling time.
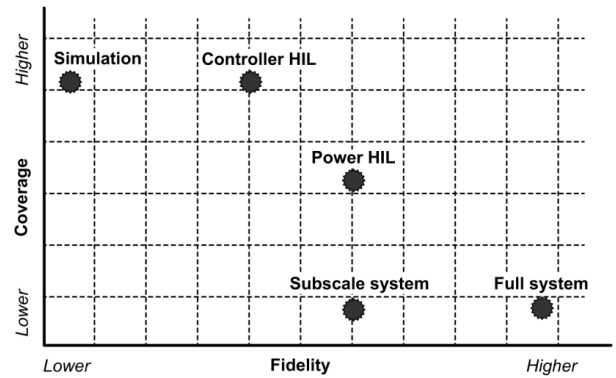

FIGURE 1. Notional comparison between power testbed types [9].

II. MMC MODEL DETAILS

The dynamic model of the converter here is fully detailed in [19]. The equivalent circuit of a three phase MMC converter is shown in Fig. 2. From the equivalent circuit, $v_{xu,l}$ is the combined voltage of the switched in SM batteries in one arm, where x is any converter phase. Here, u and l refer to the upper and the lower arms of any phase, respectively. In MMCs with an embedded capacitor in the SM, the capacitor model is relatively simple to implement, whereas in the MMC-BESS the battery model requires a considerable calculation time. An accurately represented battery model can be realised utilising the look up table method [20], [21]. For a higher number of levels per arm, including multiple look up tables is a burden on the real-time processor and decreases its performance. As a solution in this research, only one lookup table, as shown in Fig. 3, is used per arm to represent open circuit voltage, and state of charge ($v_{oc} - SOC$) relation in a battery as described in (1).

$$v_{oc} + v_d = f(SOC(i, T)) + \Delta E(T) \quad (1)$$

where $SOC(i, T)$ is dependent on the discharge current and temperature and v_d is the dynamic voltage variations in the battery. $\Delta E(T)$, is a correction voltage that is added to v_{oc} to represent the variation due to changes in the battery temperature with time. The $SOC(i, T, t)$ can be calculated as

$$SOC(i, T, t) = SOC(t_i) - \frac{\eta_{bat}}{Q_{max}} \int_{t_i}^{t} k_1(i(t)).k_2(T(t)).i(t)dt \quad (2)$$

where $\eta_{bat}(T, i(t))$ is the coulombic efficiency of the battery and $Q_{max}(T)$ is the battery maximum capacity in ampere-seconds. Correction factors k_1 and k_2 are used to describe the variations of SOC due to current discharge rate and temperature [21].

Lithium-Ion cell INR18650-25R discharge curves at 1C, 2C, 4C, and 6C, are shown in Fig. 4 [22]. The cell model is simulated at the same discharge rates as the given manufacturer data. The battery simulated curves are almost identical to the discharge data give by the manufacturer.
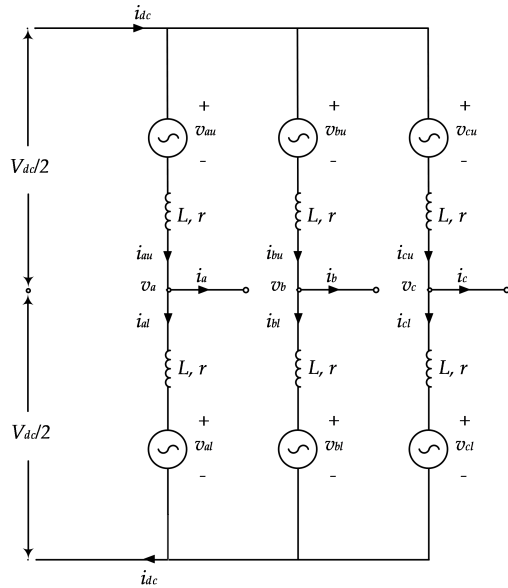
FIGURE 2. Equivalent circuit of a three phase MMC-BESS.

TABLE 1. The state variables of a SM.

S_x	S_a	STATE VARIABLES
1	0	$v_{SM} = v_{battery}$, $i_{battery} = i_{arm}$
0	1	$v_{SM} = 0$, $i_{battery} = 0$, $v_{battery} = $ unchanged

An ideal representation of SM switching as used in the converter is shown in Fig. 5. When a switch (S_x or S_a) is on, the conduction loss of this switch is neglected; the off state of the switch is considered as open circuit [23]. Therefore the switching vector s_{wv} can be written as in (3). The SM (the battery and the two switches) output voltage and current are expressed by the battery state variables during on and off status as listed in Table 1. Blocked status (both switches are off) is not represented in this research.

$$s_{wv} = \begin{bmatrix} s_{x,1} \\ s_{x,2} \\ \vdots \\ s_{x,n} \end{bmatrix} \quad (3)$$

The combined voltage of the series connected active SMs is expressed using an insertion index i. The arm voltage of switched arm NV_b can be written as

$$v_{xu,l} = \sum_{i=1}^{i=n} s_{x,i} v_{b,i} \quad (4)$$

where $s_{x,i} \in \{0, 1\}$, N is the number of SMs per arm, and v_b is the battery voltage.

Individual battery current can be calculated using the switching vector s_{wv} multiplied by the arm current.

The current vector of the SM battery current equals

$$i_B = \begin{bmatrix} i_{battery,1} \\ i_{battery,2} \\ \vdots \\ i_{battery,n} \end{bmatrix} \quad (5)$$

From the voltage calculated in (4) and the equivalent circuit in Fig. 2, the converter upper and lower arm voltage in any phase x can be written as

$$v_{xu} = \frac{V_{dc}}{2} - v_x - L\frac{di_{xu}}{dt} - ri_{xu}$$
$$v_{xl} = \frac{V_{dc}}{2} + v_x - L\frac{di_{xl}}{dt} - ri_{xl} \quad (6)$$

Also, the arm currents are

$$\left.\begin{matrix} i_{au} = \frac{i_{dc}}{3} + i_{cir,a} + \frac{i_a}{2}, \ i_{al} = \frac{i_{dc}}{3} + i_{cir,a} - \frac{i_a}{2} \\ i_{bu} = \frac{i_{dc}}{3} + i_{cir,b} + \frac{i_b}{2}, \ i_{bl} = \frac{i_{dc}}{3} + i_{cir,b} - \frac{i_b}{2} \\ i_{cu} = \frac{i_{dc}}{3} + i_{cir,c} + \frac{i_c}{2}, \ i_{cl} = \frac{i_{dc}}{3} + i_{cir,c} - \frac{i_c}{2} \end{matrix}\right\} \quad (7)$$

where $i_{cir,x} = \frac{i_{xu} + i_{xl}}{2}$ and i_{dc} is the DC current that flows between legs.

The DC voltage of the converter can be expressed by adding the upper and the lower arm voltages in (6) as

$$(V_{dc} = v_{xu} + v_{xl} + L\frac{d(i_{xu} + i_{xl})}{dt} + r(i_{xu} + i_{xl}) \quad (8)$$

Arm currents can be written in terms of the circulating current $i_{cir,x}$ and phase current i_x as

$$i_{xu} = i_{cirx} + \frac{i_x}{2}$$
$$i_{xl} = i_{cirx} - \frac{i_x}{2} \quad (9)$$

where $i_{cir,x} = \frac{i_{u,x} + i_{l,x}}{2}$

The DC voltage can be expressed as [19],

$$3V_{dc} = v_{au} + v_{al} + v_{bu} + v_{bl} + v_{cu} + v_{cl} + 2L\frac{di_{dc}}{dt} + 2ri_{dc} \quad (10)$$

and the dynamic DC current equals

$$\frac{di_{dc}}{dt} = \frac{1}{2L}\left[3V_{dc} - \sum_{x=a,b,c}(v_{xu} + v_{xl}) - 2ri_{dc}\right] \quad (11)$$

The dynamic equation of the circulating current in phase a can be derived as [19]

$$\frac{di_{cir,a}}{dt} = \frac{1}{6L}\left[\sum_{x=a,b,c}(v_{xu} + v_{xl}) - 3(v_{au} + v_{al}) - 6ri_{cir,a}\right] \quad (12)$$

similarly, the dynamic equations of the circulating currents in phase b and c can be derived. Equations (6), (9), (11), and (12) are used to to model the converter transients in HIL system.
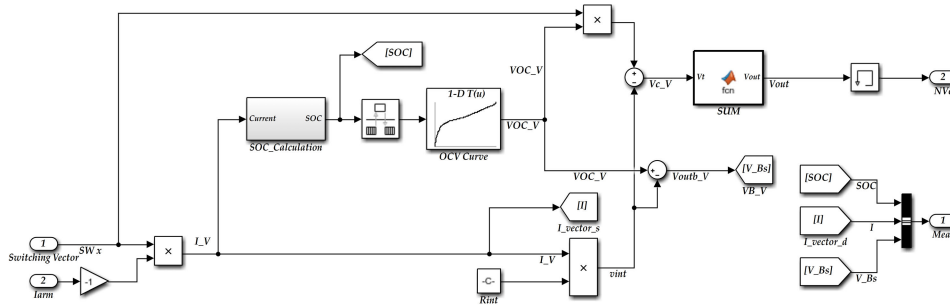
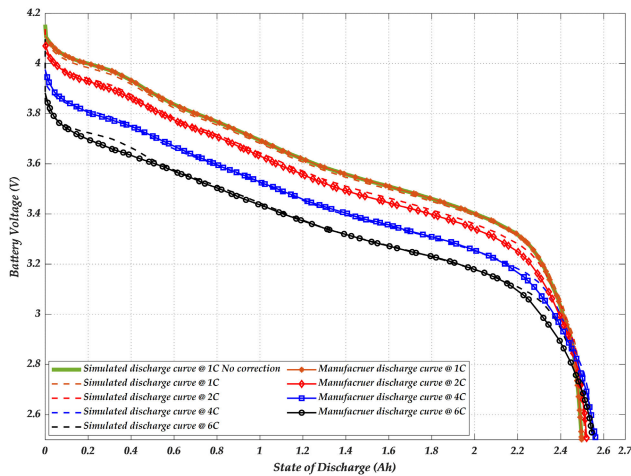**FIGURE 3.** Batteries model in one arm using a single look-up table (the OCV curve).

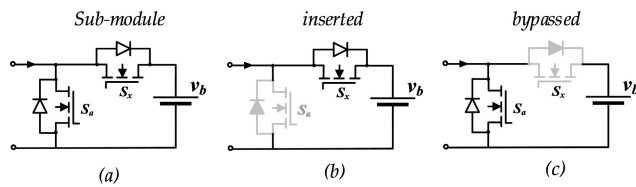**FIGURE 4.** Simulated and manufacturer battery, INR18650-25R, discharge curves at 1C, 2C, 4C, and 6C [22].

FIGURE 6. Laboratory prototype.

FIGURE 5. Submodule switching status.

III. VALIDATION OF THE CHIL REAL-TIME SYSTEM WITH A LABORATORY PROTOTYPE

An experimental MMC-BESS prototype of five voltage levels per phase is shown in Fig. 6. The converter comprises four SMs per arm. Each SM contains two MOSFETs (*NTP6412ANG*) switched by the isolated gate drivers *UCC*21520*DWR*. Only one PWM signal from the controller turns ON the main MOSFET S_a and turns OFF the auxiliary MOSFET S_x. The default of the SM is to be bypassed at low PWM input signal. Two packs of the battery block INR18650-25R manufactured by *ENEPAQ Ltd* are connected in series for each SM [24]. Both battery packs are identical and were tested for any voltage discrepancy when charged and partially discharged to confirm that the SOC of the
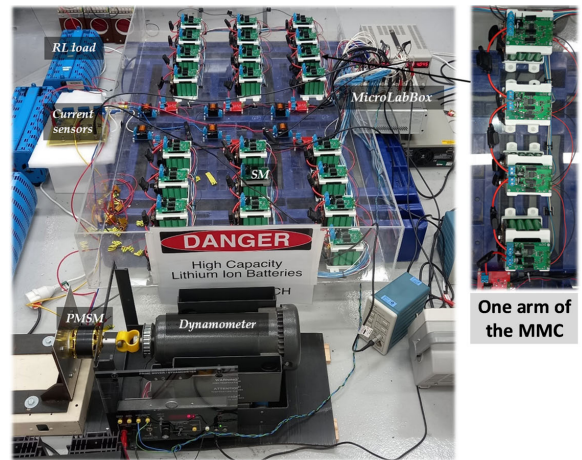
SM reflects the actual SOC of each battery. Current sensors LEM HLSR 32-P are used to measure the arm currents. The converter arm inductors minimise the circulating current. The arm inductor has another important benefit which is the limiting of transient short circuit currents in the converter arms. The prototype converter arm inductor has a datasheet value of 33 μH at 100 kHz [25]. The converter arm impedance is dependent on the frequency due to inductor core properties. As shown in Fig. 7, the arm inductor was tested at different frequency values to evaluate the proper value of an equivalent series RL connection that should be used during CHIL implementation. At 2 kHz, suitable values of $L = 41.2$ μH and $R = 0.068$ Ω are used to validate the proposed converter dynamic model. The *MicroLabBox* CHIL is used to emulate the converter operation when connected to both an RL load and when connected to a motor.

A. CONNECTION OF THE MMC-BESS TO AN RL LOAD

The converter prototype was connected to a three phase static RL load and tested for operational performance. A full account of this test is provided in [19], and summarised here. Table 2 details the converter and the RL load parameters. The RL load is modelled using the following
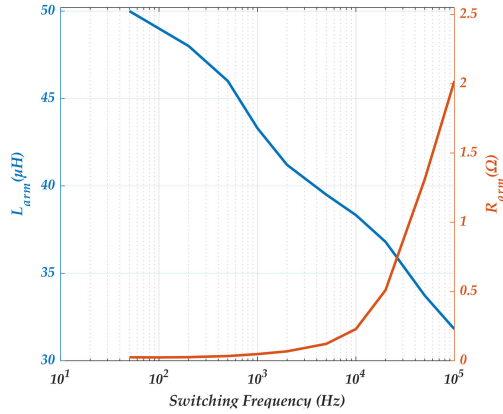
FIGURE 7. Arm inductor inductance and resistance variation with switching frequency.

dynamic equation

$$\frac{di_x}{dt} = \frac{v_x}{L_o} - \frac{R_o}{L_o} i_x \tag{13}$$

The modulation technique in this test is the Phase Shifted PWM (*PSPWM*) [6]. A simplified sorting algorithm is used to equalise the SOC of the arm SMs as shown in Fig. 8. Equalising the SOC of the batteries is essential to reduce the circulating currents that occur due to voltage differences between the arms. Therefore, the SM with a battery that has a higher SOC will be switched on when the current direction is negative in the arm, and a battery in the SM with a lower SOC will be switched on when the current is positive in that arm. The SMs that should be switched on is a sub-control algorithm of the main control, which is the terminal voltage control. The terminal voltage controller generates the reference voltage, which is then modulated and passed through the sorting algorithm. The output is a switching vector that determines which SMs are on or off based on their batteries SOC and current direction. This sorting algorithm can be extended to equalise the SOC of any number of SMs per arm. Balancing controllers that are used to equalise the average SOC of the converter legs and arms are not implemented in this test. The converter has an open loop control reference voltage with a modulation amplitude ratio of 0.8. The sampling time for the prototype and the emulated system is 40 μs and the test is conducted for 3400 seconds. The current in the upper and the lower arms of all three phases during experimental operation of the prototype and real-time CHIL emulation are shown in Fig. 9. The real-time CHIL converter dynamic performance is very close to the prototype dynamics. The upper and lower arm current waveforms are highly dependent on the arms states of charge. These are difficult to match between the two systems, and is the reason for the differences between the emulated and experimental results.

The SOC of the batteries in the converter arms is shown in Fig. 10 for the prototype and in Fig. 11 for the emulated converter. As shown in shown in Fig. 10, the prototype converter test was conducted with the SOC of the batteries in

TABLE 2. The state variables of a submodule.

Variable	Value
Nominal Battery voltage	7.2 V
Arm inductance	41.2 μH
Arm resistance	0.068 Ω
Load inductance	5.32 mH
Load resistance	5 Ω

```
if I>0
    [~,i]=sort(SOC,'ascend');
    M(i(1:N))=1;
    M(i(N+1:4))=0;
else
    [~,i]=sort(SOC,'descend');
    M(i(1:N))=1;
    M(i(N+1:4))=0;
end
```

FIGURE 8. Sorting algorithm, 4 SMs per arm.

the converter arms having different initial values. The same initial SOC values were used in the emulated system. While the operational characteristics are very similar, there are slight differences at the end of the operation between the actual and emulated batteries SOC. Reasons for these differences include current measurement error and arm resistance differences. It is assumed that all arms have the same inductance and resistance in the model, but this is not the typical case for the physical hardware. Additional deviation is due to the battery model. While the battery model is proven to be very close to the actual batteries used, battery terminal voltage and internal resistance is different from one battery to another, in addition to the measurement error of the battery voltage sensor.

B. MOTOR OPERATION

A Permanent Magnet Synchronous Motor (PMSM) operation in a real-time CHIL is compared to the prototype converter motor loaded operation. The same experimental prototype converter that has been used to test the RL load is used with the motor load. The sorting algorithm is the same sorting algorithm for the RL operation. However to control the motor, field oriented control (*FOC*) is implemented [26]. A shaft encoder is used to measure rotor position. Modelling equations of the motor for CHIL implementation can be written as [26]

$$\frac{d}{dt} i_d = \frac{v_d - R_s i_d + L_q p \omega_m i_q}{L_d}$$
$$\frac{d}{dt} i_q = \frac{v_q - R_s i_q - L_d p \omega_m i_d - \lambda_f p \omega_m}{L_q} \tag{14}$$

where d and q are the reactive and active components of the voltage and the current, λ_f is motor flux linkage, and ω_m is the rotor mechanical speed. Motor parameters are detailed in Table 3 [27]. Motor speed and current PI controllers are tuned based on the motor transfer function. This was implemented using the Matlab/Simulink PID tuner application. The motor
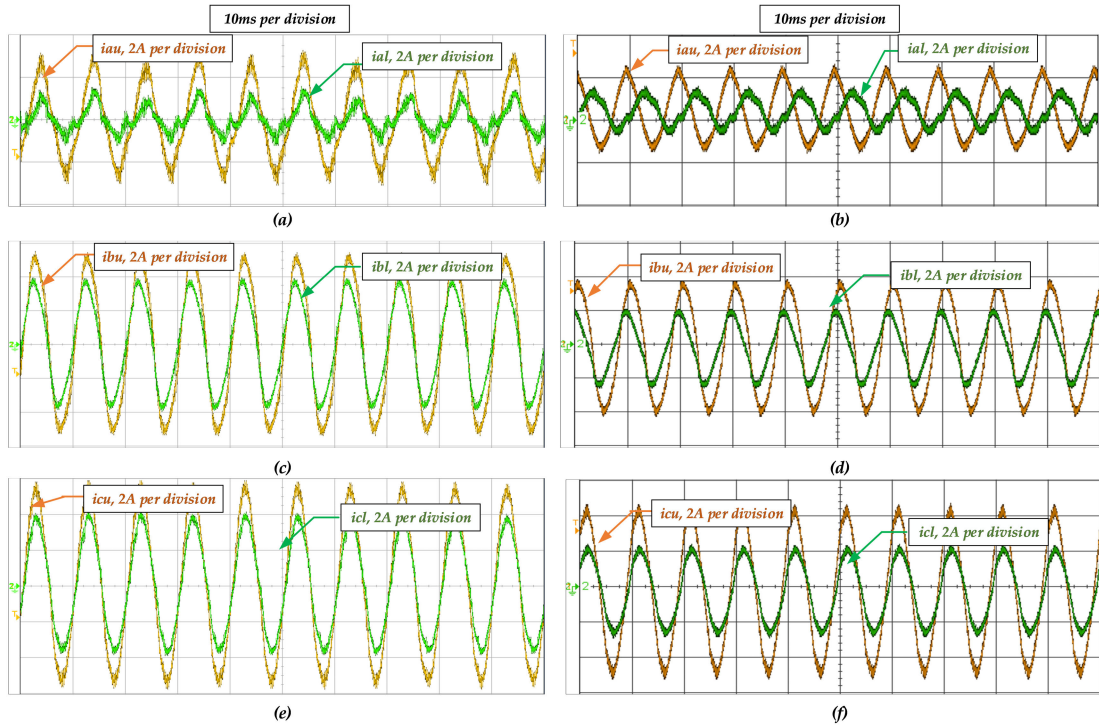
FIGURE 9. The upper and the lower arm currents in (a) phase *a* of the prototype converter, (b) phase *a* of the real-time CHIL, (c) phase *b* of the prototype converter, (d) phase *b* of the real-time CHIL, (e) phase *c* of the prototype converter, and (f) phase *c* of the real-time CHIL.
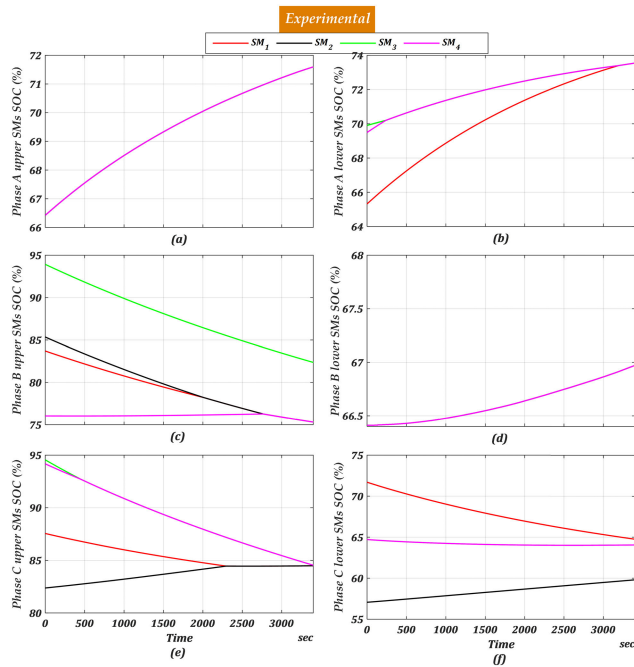

FIGURE 10. Individual batteries SOC in the prototype converter: (a) upprer arm *a*, (b) lower arm *a*, (c) upper arm *b*, (d) lower arm *b*, (e) upper arm *c*, and (f) lower arm *c*.
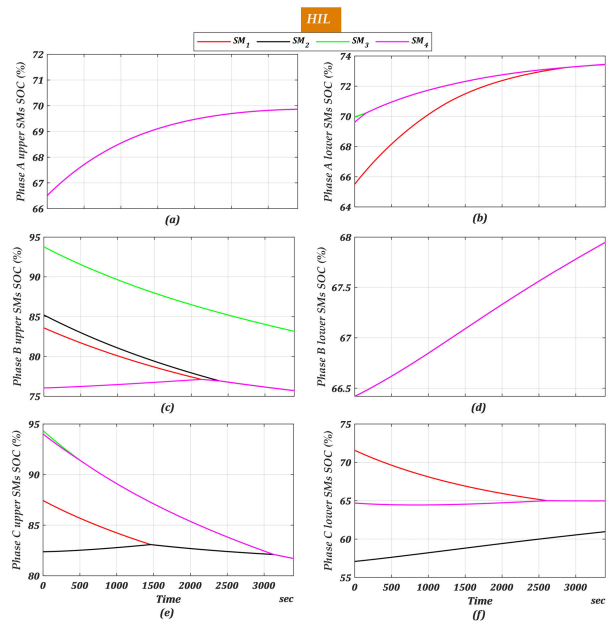

FIGURE 11. Individual batteries SOC in the real-time CHIL: (a) upprer arm *a*, (b) lower arm *a*, (c) upper arm *b*, (d) lower arm *b*, (e) upper arm *c*, and (f) lower arm *c*.

instantaneous electromagnetic torque is given by

$$T_e = 1.5\, p \left[\lambda_f i_q + \left(L_d - L_q \right) i_d i_q \right] \tag{15}$$

The mechanical and electrical torque relation of the motor is expressed as

$$T_e - T_m = J \frac{d\omega_m}{dt} + B\omega_m \tag{16}$$

TABLE 3. Small scale PMSM motor [27].

$Variable$	$Value$
Stator Resistance, R_s	0.032 Ω
Stator direct and quadrature inductance, L_d and L_q	87 μH
No. of pole pairs, p	7
Flux linkage, λ_f	0.01065
Motor inertia, J	590e-6 $kg.m^2$
Current proportional gain	0.1
Current integral gain	0.32
Speed proportional gain	0.6
Speed integral gain	1.75

where J is the rotor moment of inertia and B is the rotor friction coefficient.

Level shifted PWM is used in the motor FOC. An efficient approach is implemented in this CHIL model by utilising a global main carrier signal which will be used to determine all carriers for all SMs. The triangular global carrier has an amplitude of [1 $(1 + \frac{2}{N})$ 1] values at time values [0 $0.5/F_c$ $1/F_c$], where F_c is the carrier frequency (Hz). According to the SM number and the total number of SMs in the converter arm, a value CS is subtracted form the global carrier to shift all carrier signals in space from -1 to $+1$ as shown in (17).

$$CS = \frac{n_i}{\frac{N}{2}} \quad (17)$$

where n_i is the number index of the SM arranged from 1 to N.

This approach minimised the required calculation time of the real-time CHIL model as observed during testing. A comparison between the motor operation of the prototype and the real-time CHIL is shown in Fig. 12 and Fig. 13 respectively. The converter with motor is loaded using a dynamometer while the speed is changing. In the prototype, the motor starts from zero speed to follow the reference speed (114 rad/sec) as shown in the speed variations in Fig. 12 (a). The torque changes are shown in Fig. 12 (b). Leg a voltage is shown in Fig. 12(c), where the leg voltage is almost constant at values equal to NV_c during the complete range of the operation. Fig. 12(d) shows the reference voltage of phase a and the mechanical rotor position. The rotor position is aligned with the peak value of phase a voltage. The testing conditions of the prototype operation are repeated for the CHIL converter operation. It can be observed from Fig. 13 (a) that the speed variation is almost the same as the prototype system, except for a minor overshoot in the prototype during speed transient changes. The load torque has the same profile of the prototype as shown in Fig. 13 (b). Leg a voltage measured between the positive and the negative bus bars is shown in Fig. 13 (c). The FOC reference voltage of phase a and the rotor position are shown in Fig. 13 (d)

FOC operation of the prototype is shown in Fig. 14. The motor quadrature current component is shown in Fig. 14(a). The current reference has a positive command to accelerate the motor and has a negative command to decelerate the motor. Fig. 14(b) shows the direct component of the motor current which is controlled to be zero. Fig. 14 (c) and (d) show
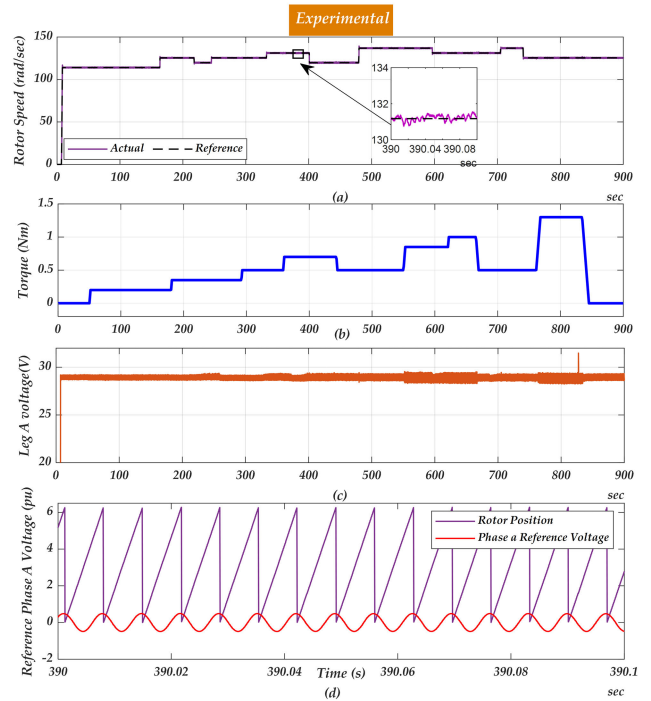

FIGURE 12. Motor operation in the prototype (a) rotor speed, (b) load torque, (c) Leg a voltage, and (d) phase a reference voltage.
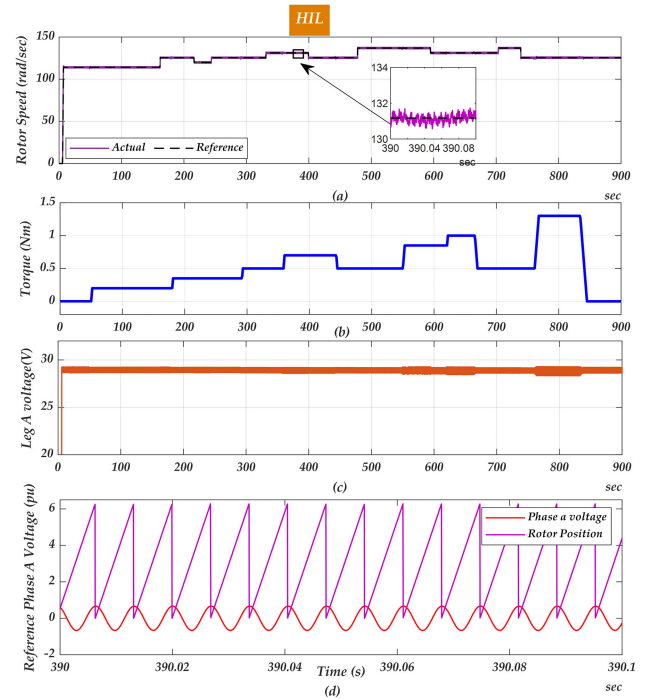

FIGURE 13. Motor operation in the real-time CHIL (a) rotor speed, (b) load torque, (c) Leg a voltage, and (d) phase a reference voltage.

the motor quadrature current and the motor current in phase a during a period of 0.1 seconds. Fig. 14 (e) shows the upper and the lower arm currents in phase a. The current variation of the CHIL is shown in Fig. 15 for i_q, i_d, phase a currents.
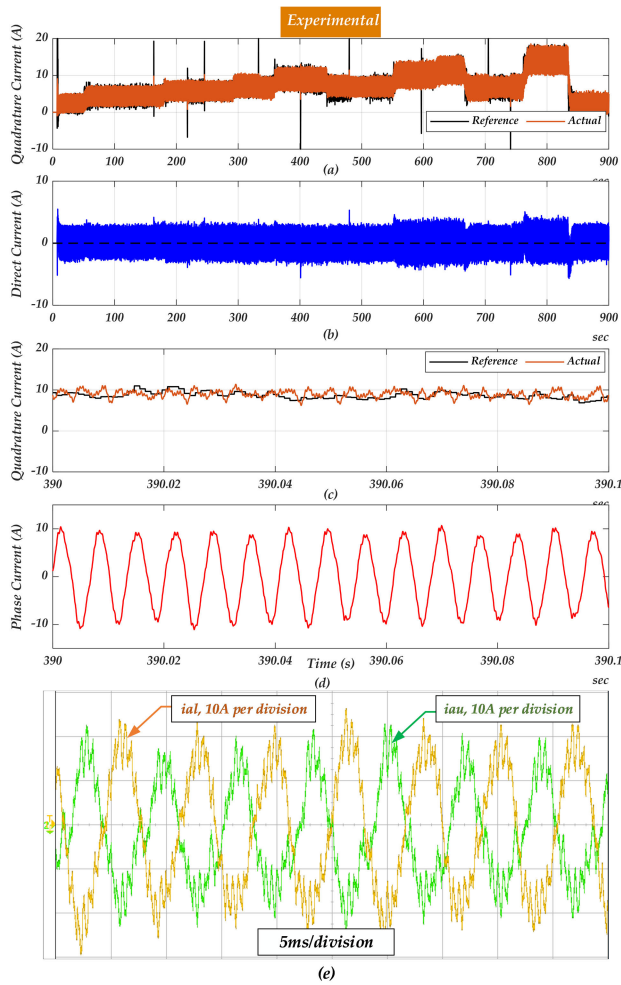
FIGURE 14. Motor operation in the prototype (a) quadrature current, (b) direct current, (c) zoomed in quadrature current (d) current in phase *a*, and (e) current in phase *a* upper and lower arms.

FIGURE 15. Motor operation in the real-time CHIL (a) quadrature current, (b) direct current, (c) zoomed in quadrature current (d) current in phase *a*, and (e) current in phase *a* upper and lower arms.

Of note here is that the arm current values in the prototype are slightly higher compared to the CHIL operation, this is a result of the measurements errors and noise interference.

The SOC of individual batteries in each arm of the converter is compared in Fig. 16 and Fig. 17. The initial SOC of the batteries in the converter upper arms are lower than those in the lower arms. Therefore, there is a slightly lower current amplitude in the upper arm compared to the lower arm current in phase *a* as shown in Fig. 14 (e). A first order low pass filter with a cut off frequency = 400 *Hz*, is used to reduce noise in the arm currents in the CHIL as shown in Fig. 15 (e). The higher the arm current, the faster equalisation of the batteries' SOC. Sub-figures (b), (d), and (f) in Fig. 16 and Fig. 17 show the faster SOC balancing operation.

The general trend of the batteries SOC shows that the sorting algorithm and the equalisation performance is a credible technique regardless the minor difference between final values of the SOC which is highly dependent on the measurement of the arm currents and noise.
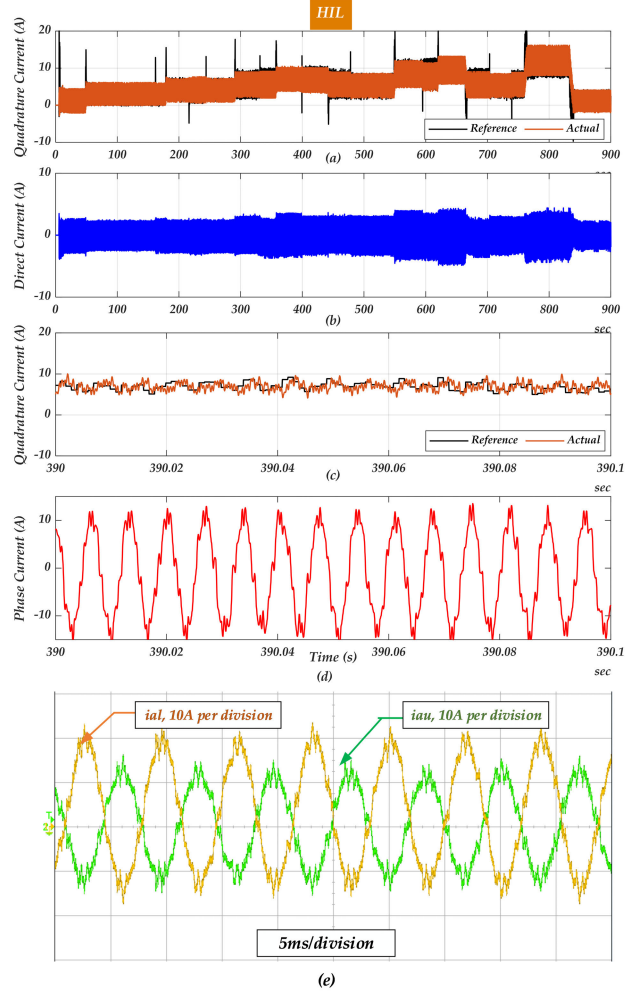
IV. EXTENSION OF REAL-TIME CHIL TO HIGH NUMBER OF SMS PER ARM

The developed real-time CHIL model is validated in section III. This gives confidence to further investigate the converter operation, control methods, and the motor dynamic behaviour. The sorting algorithm shown in Fig. 8 can be seamlessly extended to 40 SMs per arm via changing the maximum number of levels in the loop. The battery model is based on vector representation, which enables extension to any number of levels. However, this is limited by the hardware capabilities of *MicroLabBox/dSPACE* to emulate real-time operation of the converter without task overrun. Here the CHIL utilises only one *MicroLabBox/dSPACE* to eliminate the need for DIOs that are required between the CHIL platform and the controller. Implementing the converter, control system with the sorting algorithm, and the motor dynamics in the same platform adds a burden on the *MicroLabBox/dSPACE* real-time operation. Therefore, a 40 SMs/arm MMC-BESS system is emulated to test a larger
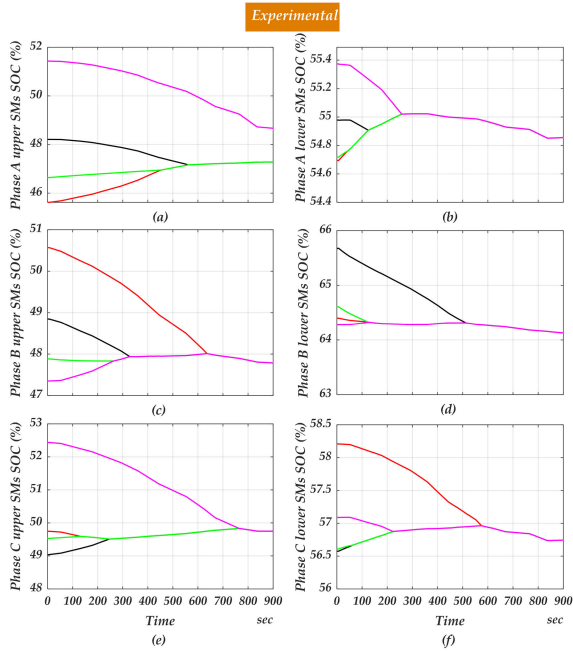
FIGURE 16. Individual batteries SOC in the prototype converter at loading condition, small scale motor: (a) upprer arm *a*, (b) lower arm *a*, (c) upper arm *b*, (d) lower arm *b*, (e) upper arm *c*, and (f) lower arm *c*. (loaded motor operation).

FIGURE 17. Individual batteries SOC in the real-time CHIL at loading condition, small scale motor: (a) upprer arm *a*, (b) lower arm *a*, (c) upper arm *b*, (d) lower arm *b*, (e) upper arm *c*, and (f) lower arm *c*. (loaded motor operation).
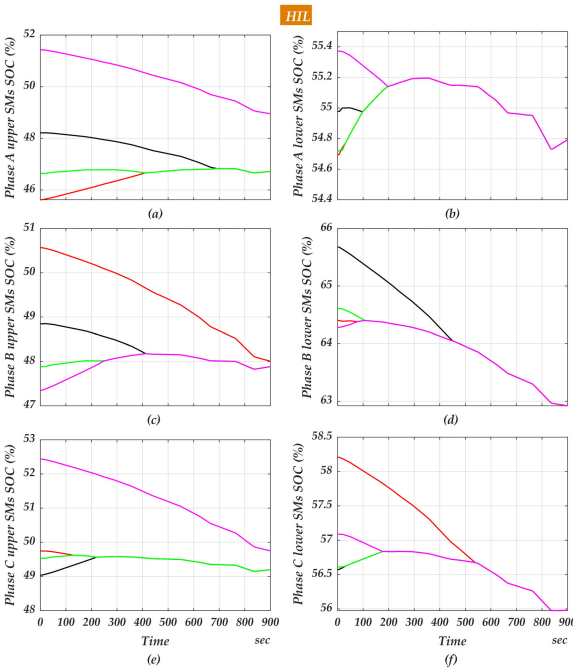
scale motor. The parameters of the motor under test are shown in Table 4 [28].

The converter operation was tested under loaded motor conditions and variable speed operation for 3700 seconds.

TABLE 4. Large scale PMSM motor [28].

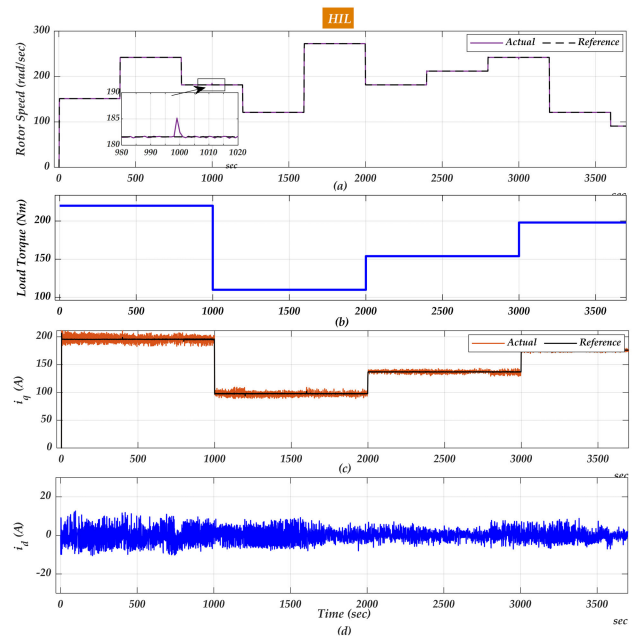| Variable	Value
Stator Resistance, R_s	$0.04\ \Omega$
Stator direct and quadrature inductance, L_d and L_q	$0.3\ mH$
No. of pole pairs, p	6
Flux linkage, λ_f	$0.125\ Wb$
Motor inertia, J	$0.05\ kg.m^2$
Current proportional gain	1.0
Current integral gain	20.0
Speed proportional gain	1.06
Speed integral gain	5.95
Motor Nominal Power	$75\ kW$
Motor Nominal Torque	$220\ Nm$

FIGURE 18. Motor operation in real-time CHIL at different load torque values (a) Rotor Speed, (b) load torque, (c) quadrature current, and (d) direct current.

Motor speed change is shown in Fig. 18 (a). Changes in quadrature (active) current component are shown in Fig. 18 (c) according to the torque changes in Fig. 18 (b). Fig. 18 (d) is controlled to be zero during different load and speed changes. Motor speed is shown to be very stable under changing load conditions. In this test, the initial SOC of the the converter batteries range from 50 to 90 % in phase *a* upper arm as shown in Fig. 19(b). This very wide SOC range is used to confirm the efficacy of the sorting algorithm. The average SOC of the converter legs and arms were naturally balanced during the motor operation. It is advised to control the SOC of the legs and the arms by a dedicated method as presented in [6] to minimise circulating currents. The emulated motor terminal voltages of phase *a*, *b*, and *c* are shown in Fig. 20(a). The high number of SMs provides a close reproduction of a sinusoidal waveform. The emulated motor voltage was captured using an oscilloscope to show that the converter dynamics can be interfaced in real-time devices for the purpose of measurement or integration. The Motor phase current
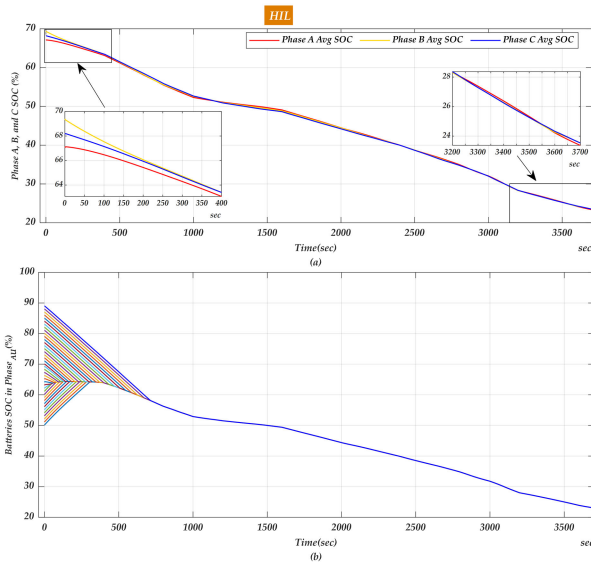
FIGURE 19. Motor operation in the real-time CHIL at different load torque values (a) Legs average SOC, (b) individual batteries SOC in phase *a* upper arm.
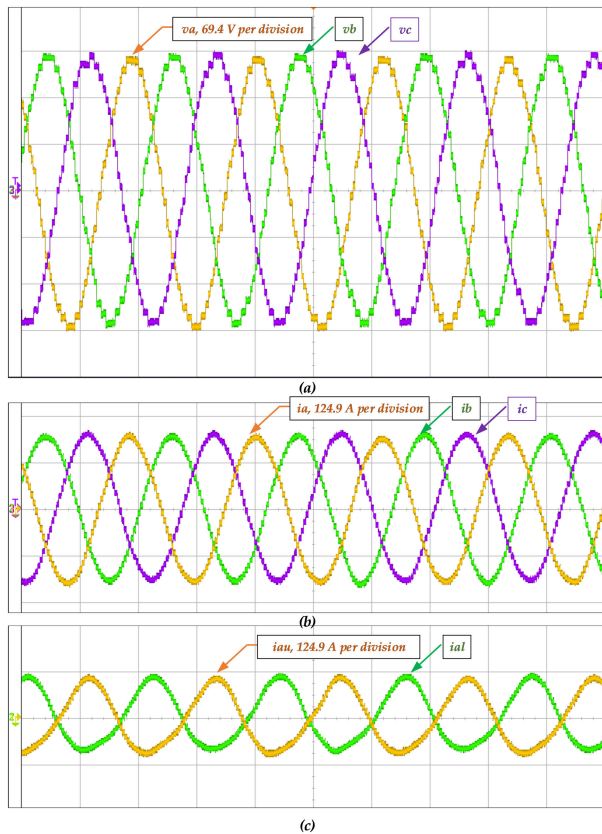

FIGURE 20. Motor operation in the real-time CHIL at different load torque values (a) phase *a*, *b* and *c* voltage, (b) phase *a*, *b* and *c* current, and (C) current in the upper and lower arms of phase *a*.

is shown in Fig. 20(b). Again, the high number of SMs results in close reproduction of a sinusoidal waveform. Fig. 20(c) shows currents in phase *a* upper and lower arms. Currents are

captured when the SOC of the batteries in the upper and in the lower arms were almost balanced, and circulating current was small.

V. CONCLUSION

The real-time CHIL of the MMC-BESS presented its merits regarding facilitating investigation of the converter dynamic performance. While there are minor deviations between the prototype and the real-time emulation system values, the CHIL system is able to demonstrate high fidelity performance during different loads and operational conditions. The most important aspect of the proposed system is that it can be easily extended and interfaced to any number of levels without significant change in the converter basic structure or the sorting algorithm arrangement. When it comes to interfacing of high number of IOs, Ethernet or Fibre connection can be established to transfer the switching commands from the controller to the hosting platform. Also, the system can be connected to an EV emulator to test the dynamics of the vehicle and the converter performance. Based on this study, further investigation can be implemented by splitting the converter and the control system. Ethernet connection can be tested for high speed transfer of the data from the controller to the converter. Various balancing approaches of the converter average SOCs can be investigated using the same converter emulation system. While not part of this study, possible long term battery issues due to current ripple could possibly be mitigated through use of capacitors or different SM topology.

REFERENCES

[1] M. Spichartz, V. Staudt, and A. Steimel, "Analysis of the module-voltage fluctuations of the modular multilevel converter at variable speed drive applications," in *Proc. 13th Int. Conf. Optim. Electr. Electron. Equip. (OPTIM)*, Brasov, Romania, May 2012, pp. 751–758, doi: 10.1109/OPTIM.2012.6231806.

[2] Siemens. *M2C-Technology*. Accessed: May 29, 2023. [Online]. Available: https://www.siemens.com/global/en/products/drives/sinamics/medium-voltage-converters/m2c-technology.html

[3] N. Ahmed, A. Haider, D. Van Hertem, L. Zhang, and H. Nee, "Prospects and challenges of future HVDC SuperGrids with modular multilevel converters," in *Proc. 14th Eur. Conf. Power Electron. Appl.*, Birmingham, U.K., Aug. 2011, pp. 1–10.

[4] S. Ali, J. B. Soomro, M. Mughal, F. A. Chachar, S. S. H. Bukhari, and J. Ro, "Power quality improvement in HVDC MMC with modified nearest level control in real-time HIL based setup," *IEEE Access*, vol. 8, pp. 221712–221719, 2020, doi: 10.1109/ACCESS.2020.3043811.

[5] H. Saad, T. Ould-Bachir, J. Mahseredjian, C. Dufour, S. Dennetiere, and S. Nguefeu, "Real-time simulation of MMCs using CPU and FPGA," *IEEE Trans. Power Electron.*, vol. 30, no. 1, pp. 259–267, Jan. 2015, doi: 10.1109/TPEL.2013.2282600.

[6] A. Omar, A. Wood, H. Laird, and P. Gaynor, "Simplified SOC balancing of an MMC with embedded storage in an EV system," in *Proc. IEEE Region Conf. (TENCON)*, Dec. 2021, pp. 929–934, doi: 10.1109/TENCON54134.2021.9707466.

[7] M. Quraan, T. Yeo, and P. Tricoli, "Design and control of modular multilevel converters for battery electric vehicles," *IEEE Trans. Power Electron.*, vol. 31, no. 1, pp. 507–517, Jan. 2016.

[8] N. Li, F. Gao, T. Hao, Z. Ma, and C. Zhang, "SOH balancing control method for the MMC battery energy storage system," *IEEE Trans. Ind. Electron.*, vol. 65, no. 8, pp. 6581–6591, Aug. 2018, doi: 10.1109/TIE.2017.2733462.

[9] *IEEE Standard for the Testing of Microgrid Controllers*," Standard 2030.8-2018, 2018, doi: 10.1109/ieeestd.2018.8444947.

[10] H. Magnago, H. Figueira, O. Gagrica, and D. Majstorovic, "HIL-based certification for converter controllers: Advantages, challenges and outlooks (invited paper)," in *Proc. 21st Int. Symp. Power Electron. (EE)*, Oct. 2021, pp. 1–6.

[11] W. Li, L. Gregoire, P. Robert, S. Souvanlasy, and J. Belanger, "Modular multilevel converter model implemented in FPGA for HIL test of industrial controllers," in *Proc. IEEE PES Gen. Meeting Conf. Expo.*, Jul. 2014, pp. 1–5.

[12] M. Ricco, L. Mathe, E. Monmasson, and R. Teodorescu, "FPGA-based implementation of MMC control based on sorting networks," *Energies*, vol. 11, no. 9, p. 2394, Sep. 2018.

[13] W. Wu, X. Wu, L. Jing, and J. Li, "Design of modular multilevel converter Hardware-in-Loop platform based on RT-lab," in *Proc. IEEE 8th Int. Power Electron. Motion Control Conf. (IPEMC-ECCE Asia)*, May 2016, pp. 2350–2355.

[14] P. Bontemps, S. Milovanovic, and D. Dujic, "Virtual capacitor concept for partitioning of large converter systems for RT-HIL simulations," in *Proc. Int. Power Electron. Conf.*, May 2022, pp. 1801–1808.

[15] C. Dong, W. Yankun, M. Yulong, Y. Pingping, and W. Zhipeng, "Real time digital simulation and HIL test of Xiamen MMC-HVDC demonstration project," in *Proc. Int. High Voltage Direct Current Conf. (HVDC)*, 2016, pp. 1–5.

[16] OPAL-RT. *Modular Multilevel Converter (MMC) Test Bench*. Accessed: Mar. 14, 2023. [Online]. Available: https://www.opal-rt.com/mmc-test-bench/

[17] W. C. S. Amorim, J. V. G. França, A. F. Cupertino, V. F. Mendes, and H. A. Pereira, "Mission profile emulator for mmc-based battery energy storage systems," *Eletrônica de Potência*, vol. 27, no. 2, pp. 177–185, Jun. 2022, doi: 10.18618/rep.2022.2.0035.

[18] L. Leister, A. Kalk, B. Schmitz-Rode, L. Stefanski, D. Bräckle, and M. Hiller, "Hardware-in-the-loop setup for a modular multilevel converter with integrated batteries," in *Proc. IEEE 23rd Workshop Control Model. Power Electron. (COMPEL)*, Jun. 2022, pp. 1–7, doi: 10.1109/COMPEL53829.2022.9830034.

[19] A. Alaa, A. Omar, A. Wood, H. Laird, and P. Gaynor, "Real-time emulation of a MMC with BESS for EV application," Aug. 2022, pp. 1–6, doi: 10.46855/energy-proceedings-10021.

[20] L. Gao, S. Liu, and R. A. Dougal, "Dynamic lithium-ion battery model for system simulation," *IEEE Trans. Compon. Packag. Technol.*, vol. 25, no. 3, pp. 495–505, Sep. 2002.

[21] J. Schonberger, "Modeling a lithium-ion cell using PLECS," *Plexim GmbH*, pp. 1–5, Jan. 2009.

[22] Samsung SDI, "Specification of product lithium-ion rechargeable cell for power tools model name," Spec. No. INR18650-25R, South Korea, 2014.

[23] H. Saad, C. Dufour, J. Mahseredjian, S. Dennetiere, and S. Nguefeu, "Real time simulation of MMCs using the state—Space nodal approach," in *Proc. IPST*, 2013, pp. 17–20.

[24] Enepaq. *Battery Modules*. Accessed: Mar. 15, 2023. [Online]. Available: https://enepaq.com/product-category/battery-modules/

[25] WÜRTH ELEKTRONIK. *WE-HCFT THT High Current Inductor*. Accessed: May 29, 2023. [Online]. Available: https://www.we-online.com/en/system/search?sword=7443763540330

[26] P. Krause, O. Wasynczuk, S. Sudhoff, and S. Pekarek, *Analysis of Electric Machinery and Drive Systems*. Hoboken, NJ, USA: Wiley, Jun. 2013, doi: 10.1002/9781118524336.

[27] *Scorpion SII-6530-150KV*. Accessed: May 29, 2023. [Online]. Available: https://www.scorpionsystem.com/catalog/aeroplane/motors_1/sii-65/SII-6530-150KV/

[28] *AFM-140 Axial Flux Motor*. Accessed: May 29, 2023. [Online]. Available: https://www.yumpu.com/en/document/view/16515355/afm-140-axial-flux-motor-afm-140-specification-evo-electric

ALAA OMAR (Student Member, IEEE) received the B.Sc. degree in electrical engineering from Alazhar University, Cairo, Egypt, in 2009, and the M.Sc. degree from Cairo University, Giza, Egypt, in 2015. He is currently pursuing the Ph.D. degree with the University of Canterbury, Christchurch, New Zealand. His research interests include MMC converters and EV drives.

ALAN WOOD (Member, IEEE) received the B.E. (Hons.) and Ph.D. degrees in electrical and electronic engineering from the University of Canterbury, Christchurch, New Zealand, in 1981 and 1993, respectively. He is currently an Associate Professor with the University of Canterbury. His research interests include power system harmonic and transient analysis, FACTS devices, modeling, control, and interactions.

HAMISH LAIRD (Senior Member, IEEE) received the B.E. and Ph.D. degrees in electrical and electronic engineering from the University of Canterbury, Christchurch, New Zealand, in 1990 and 2001, respectively. He is currently an Adjunct Staff Member with the Electrical and Computer Engineering School, Canterbury University. His research interests include FPGA for power electronics and DSP power electronics.

PAUL GAYNOR (Member, IEEE) received the B.E. (Hons.) and Ph.D. degrees in electrical and electronic engineering from the University of Canterbury, Christchurch, New Zealand, in 1990 and 1994, respectively. He is currently an Associate Professor with the University of Canterbury. His research interests include power electronics for small-scale renewable/sustainable applications and biomedical devices.

• • •